Rapid Communications

Regulating lamellar eutectic trajectory through external perturbations

Ang Zhang,[1] Jinglian Du,[1] Zhipeng Guo,[2,*] Qigui Wang,[3] and Shoumei Xiong[1,4,†]
[1]*School of Materials Science and Engineering, Tsinghua University, Beijing 100084, China*
[2]*Institute for Aero Engine, Tsinghua University, Beijing 100084, China*
[3]*Materials Technology, GM Global Propulsion Systems, Pontiac, Michigan 48340-2920, USA*
[4]*Key Laboratory for Advanced Materials Processing Technology, Ministry of Education, Tsinghua University, Beijing 100084, China*

(Received 22 April 2020; accepted 1 June 2020; published 22 June 2020)

The present understanding of asymmetric lamellar eutectics focuses on pure diffusive transport, and how the external perturbations cause asymmetric pattern transitions remains unclear. In this work, the effect of external perturbations is discussed in terms of both thermal and convective effects via phase-field modeling. The presence of thermal perturbation distorts eutectic lamellae, while the convective perturbation causes a tilt band. Both can adjust the eutectic trajectory to accommodate newly established thermodynamics by reconstructing the transport equilibrium. Furthermore, how to regulate the eutectic growth (eutectic colony, zigzag, and snakelike patterns) by altering external perturbations is investigated, which provides information on how to control eutectic evolution.

DOI: 10.1103/PhysRevE.101.061301

Prediction and control of eutectic microstructures is challenging in material metallurgy and applied physics [1,2]. The competition between interfacial capillarity and solute transport near the growth front determines the long-range periodicity of lamellar eutectics and thus influences properties of materials [3]. Most research on lamellar eutectics is established on symmetry-pattern approximation without external perturbations, i.e., the lamellar trajectories are ideally perpendicular to the growth front. However, limited studies have been performed on understanding the asymmetric eutectic pattern, e.g., the tilting pattern in many directionally solidified eutectics [4,5]. To date, compelling viewpoints in exploring the asymmetric mechanism of lamellar eutectics can be categorized into four groups: sudden increase of driving force [6,7], anisotropic interphase boundaries [8,9], different segregation behaviors of eutectic components [10,11], and unequal interface energies [12]. The eutectic changes the trajectory to accommodate newly established thermodynamic equilibrium. However, all four viewpoints are based on pure diffusive transport, i.e., neglecting thermal and/or convective effects which cannot be avoided in terrestrial experiments. The presence of external perturbations can change thermal and/or convective effects and then affect eutectic dynamics, but the underlying physics under such perturbations is less explored.

Limited experiments have been performed to explore the possible behavior and underlying mechanism. Akamatsu *et al.* [3] found that the thermal perturbation resulting from a laser spot could cause a localized depression on the lamellae growth front. Li *et al.* [13] found that the convective perturbation caused by a strong magnetic field led to morphological instability and deformation of lamellar eutectics. The external perturbations can be summarized as the interference on the thermal and/or flow field in the undercooled melt. However, the inadequate discussion and unclear mechanism under the multiphysical fields hinder the further application of external perturbations in eutectic regulation.

In practice, both thermal transport and microconvection are difficult to control. Accordingly, we adopt a standard computational approach named the phase-field model (PFM) to reveal the underlying physics. The thermal perturbation is achieved by imposing a thermal-shock perturbation into a eutectic system, similar to the application of a laser spot in Ref. [3]. The convective perturbation is imposed by introducing an external force to induce flow. The thermal-convection coupling is explicitly realized by incorporating the flow velocity into Eq. (4), and a typical simulation result is provided in Appendix A.

Based on thermodynamics, the PFM has been widely used to simulate dendritic [14,15] and eutectic [16,17] evolution. Both thermal and convective transports are solved using a kinetic-based lattice-Boltzmann model which is reduced to the macroscopic continuum equations by the Chapman-Enskog expansion [18]. Detailed formulation, discretization, and numerical validation can be found elsewhere [19,20], and only main features are presented here:

$$F = \int \sum_{j>i} \sum_{i} \left(-\frac{\varepsilon_{ij}^2}{2} \nabla\phi_i \cdot \nabla\phi_j + \omega_{ij}\phi_i\phi_j \right) + \sum_i \phi_i f^i(C_i, T) + \lambda_L \left(\sum_i \phi_i - 1 \right), \tag{1}$$

$$\partial_t \phi_i = -\frac{2}{n} \sum_{j\neq i}^{n} s_i s_j M_{ij} \left(\frac{\delta F}{\delta \phi_i} - \frac{\delta F}{\delta \phi_j} \right), \tag{2}$$

*Corresponding author: zhipeng_guo@mail.tsinghua.edu.cn
†Corresponding author: smxiong@tsinghua.edu.cn

$$\partial_t C + \phi_3 \boldsymbol{v}\cdot\nabla C = \nabla\cdot D\sum_i \phi_i \nabla C_i, \tag{3}$$

$$\partial_t T = \alpha\nabla^2 T + \frac{L}{c_p}\partial_t f_s - \dot{q}, \tag{4}$$

where F is the energy functional, including bulk energy and interfacial energy, and $\phi_i (i = 1, 2, 3)$ represents the phase-field variables varying between 0 and 1, which denotes local volume fraction of the respective phase. λ_L is the Lagrange multiplier accounting for the constraint that the sum of ϕ_i maintains at 1, ε_{ij} is the gradient energy coefficient, and ω_{ij} is the height of the double well potential. $f^i(C_i, T)$ is the free energy density with concentration C_i under temperature T, and s_i is a step function, i.e., $s_i(x,t) = 0$ if $\phi_i = 0$ and $s_i(x,t) = 1$ otherwise. $n = \sum_i s_i$, M_{ij} is the phase-field mobility, $\boldsymbol{v}$ is the flow velocity, and D is the solute diffusivity. The concentration of the system is determined by a weighted average, i.e., $C(x,t) = \sum_i \phi_i C_i$. α is the thermal diffusivity, L is the latent heat, c_p the specific heat, and $f_s = 1 - \phi_3$ is the solid fraction. $\dot{q} > 0$ is an imposed heat sink to simulate the heat flux out of the domain.

The lattice-Boltzmann equations governing both temperature and flow velocity are expressed as

$$f_i(\boldsymbol{r} + \boldsymbol{c_i}\delta t, t + \delta t) = f_i(\boldsymbol{r}, t) - \left[f_i(\boldsymbol{r}, t) - f_i^{eq}(\boldsymbol{r}, t)\right]/\tau + G_i(\boldsymbol{r}, t)\delta t, \tag{5a}$$

$$\text{with}\quad f_{i,T}^{eq} = w_i T,$$

$$f_{i,v}^{eq} = w_i\rho\left(1 + \frac{3\boldsymbol{c_i}\cdot\boldsymbol{v}}{c^2} + \frac{9(\boldsymbol{c_i}\cdot\boldsymbol{v})^2}{2c^4} - \frac{3\boldsymbol{v}\cdot\boldsymbol{v}}{2c^2}\right), \tag{5b}$$

where f_i is the particle distribution function at position $\boldsymbol{r}$ and time t, τ is the relaxation time, and $f_{i,T}^{eq}$ and $f_{i,v}^{eq}$ are the equilibrium distribution functions for temperature and flow velocity, respectively. c is the lattice speed, $\boldsymbol{c_i}$ is the discrete velocity, which is dependent on the employed 2D nine-velocity (D2Q9) model, and w_i is the weight coefficient to guarantee the conservation of mass and momentum [18]. $G_i(\boldsymbol{r}, t)$ is the discrete force with second-order accuracy and is expressed as $G_{i,T}$ and $G_{i,v}$ for temperature and flow velocity, respectively [21,22]:

$$G_{i,T} = \left(1 - \frac{1}{2\tau}\right) w_i\left(-\frac{L}{c_p}\partial_t\phi_3 - \dot{q}_{LBM}\right), \tag{6}$$

$$G_{i,v} = \left(1 - \frac{1}{2\tau}\right) w_i\left(\frac{3(\boldsymbol{c_i} - \boldsymbol{v})}{c^2} + \frac{9(\boldsymbol{c_i}\cdot\boldsymbol{v})\boldsymbol{c_i}}{c^4}\right)\cdot \times (\boldsymbol{G_D} + \boldsymbol{G_F}), \tag{7a}$$

$$\text{with}\quad \boldsymbol{G_D} = -2\rho\upsilon_k h\phi_3(1-\phi_3)^2\boldsymbol{v}/W_0^2,$$

$$\boldsymbol{G_F} = A(t)\rho\phi_3\boldsymbol{e},\quad \rho = \sum_i f_i, \tag{7b}$$

where $\boldsymbol{G_D}$ is the dissipative drag force to satisfy a no-slip boundary condition at the growth front [23], $\upsilon_k = c^2\delta t(2\tau - 1)/6$ is the kinematic viscosity, $h = 2.757$ is a dimensionless constant, W_0 is the interface thickness, $\boldsymbol{G_F}$ is the imposed lateral force driving flow [19], $A(t)$ is the force amplitude, which is dependent on the simulation time t, and $\boldsymbol{e}$ is the unit vector along the x^+ direction (i.e., parallel to the growth front). Accordingly, the macro temperature and flow velocity are [21,22]

$$T = \sum_i f_i + \frac{\delta t}{2}\left(-\frac{L}{c_p}\partial_t\phi_3 - \dot{q}_{LBM}\right), \tag{8}$$

$$\boldsymbol{v} = \sum_i f_i\boldsymbol{c_i}/\rho + (\boldsymbol{G_D} + \boldsymbol{G_F})\delta t/(2\rho). \tag{9}$$

At each advancing step, after the phase-field variables are updated by solving Eq. (2), the temperature and flow velocity are determined by solving Eqs. (5a)–(9) before updating the solute field via Eq. (3). The nonlinear governing equations are solved on a massively parallel and adaptive-mesh-refinement platform (see the detail in Appendix B).

The mesh size and initial lamellar spacing are 0.2 and 12.8 μm, respectively. Four lamellar couples with the same height of 3 μm are initialized at the bottom of the square domain. The initial undercooling is 1 K, and the material parameters are based on the Al-Cu eutectic alloy [24]. To focus on the mechanism under external perturbations, the anisotropy of interphase boundaries is ignored and the interface energy remains unchanged. Periodic boundary conditions are set at two sidewalls for all variables including phase fields, solute concentration, temperature, and velocity. Zero Neumann boundary conditions are set at both top and bottom sides for phase fields, solute concentration, and temperature. For velocity, a no-slip boundary condition is set at the bottom boundary, while a specular reflection boundary condition is applied at top to simulate free shear flow. A bounce-back scheme is employed at the moving solid/liquid interface where the solid fraction exceeds 0.9 [19].

Figure 1 shows the eutectic pattern transition under thermal and convective perturbations. The presence of a laser spot at the domain center distorts the solid-liquid interface [see Fig. 1(a)], while the left-to-right shear flow tilts the lamellae downstream [see Fig. 1(d)]. The depression of the central interface under laser-spot thermal perturbation indicates the change of both lamellar growth direction and velocity, which agrees with the experiment reported by Akamatsu *et al.* [3]. Figure 1(b) shows the eutectic contours under different heat sinks at the same time, and Fig. 1(c) shows the curving degree [see the definition of angle θ in Fig. 1(a)] varying with the heat sink. A larger heat sink corresponds to a faster growth velocity and it is easier to trigger the asymmetric transition, i.e., a large curving degree can be expected in the early simulation stage.

In Fig. 1(d), the eutectic lamellae move sideways and a straight but tilting interphase boundary is left in the solid, which agrees well with those simulated by Siquieri and Emmerich [25] and Wang *et al.* [26]. The shear flow makes the asymmetric tilt band exhibit a certain misorientation angle φ with respect to the original growth direction, but it keeps the lamellar spacing unchanged, indicating the negligible effect of convection on lamellar spacing in eutectic alloy, which agrees well the experiment reported by Lee *et al.* [27]. Figure 1(e) shows the eutectic contours extracted by setting the indicator of the α phase (ϕ_1) to 0.5, and Fig. 1(f) shows the maximum tilting angle φ versus the flow velocity at the domain top (i.e., maximum flow velocity). A stronger shear flow causes a more significant lateral drift and larger tilting degree.

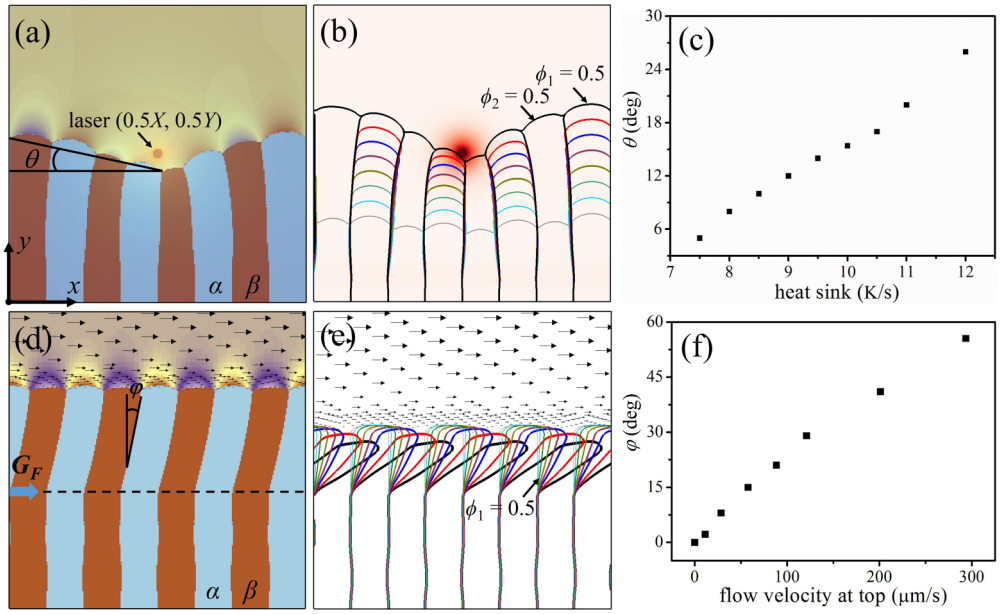

FIG. 1. Pattern transition of the eutectic lamellae under thermal and convective perturbations. The α and β phases in the cloud maps are depicted by two colors, and the black arrows in the upper remaining liquid denote the velocity vectors. (a) Cloud map of the solute field superimposed on the temperature field. (b) Eutectic contours under different heat sink. (c) Curving degree θ vs the heat sink. (d) Cloud map of the solute field under convection. (e) Eutectic contours under different convective intensity. (f) Maximum tilting angle φ vs the flow velocity at top.

Figure 2 shows the schematic diagram of the adjusting mechanism under thermal and convective perturbations. The presence of thermal perturbation in Figs. 2(a)–2(c) makes the original horizontal isotherms become curved, which changes both growth direction and growth velocity of the temperature-dependent lamellae. Figure 2(d) shows the temperature versus the distance along the horizontal direction spanning the center of the laser spot in Fig. 1(a). The nonlinear temperature distribution differs the solidification driving force among the lamellae. A lower temperature drives a faster growth velocity, forming a curved growth front [see Fig. 1(a)].

The convective perturbation changes the lamellar trajectory by changing solute transport. The lamellae grow upward vertically under the control of the solute transport couple I_1-II_1 without convection [see Fig. 2(f)]. The left-to-right shear flow strengthens the solute transport I_1 but weakens II_1, forming a transient transport couple I_m-II_m [see Fig. 2(g)]. The transient transport couple (I_m-II_m) changes the solute distribution near the growth front and shifts the eutectic components entirely downstream until reaching a steady state as designated by I_2-II_2. It is noted that the solute transport is on a similar length scale to that of the microstructure [25], and slight adjustment of the solute distribution can influence the morphological transition. During eutectic solidification, the lateral solute transfer, which is made visible near the growth front in Figs. 1(a) and 1(d), maintains the cooperative growth of the coexisting phases. When the steady transport couple changes from I_1-II_1 to I_2-II_2, the lamellae tilt downstream to accommodate such alteration [see Fig. 2(h)]. Besides, it is noted that such a single-direction tilting pattern is dependent on the side boundary condition, and the periodic side boundary condition in this work eliminates the effect of the sidewall [19]. The solute concentration without convection exhibits a sinusoidal form near the growth front, i.e., the solute concentration in liquid reaches the minimum and maximum at the centerlines of the β and α phases, respectively. The presence of convection shifts the concentration isoline towards the downstream side [28,29], and Fig. 2(e) shows the position of the concentration extremes and the leftmost triple point versus time after generating the shear flow (focusing on the leftmost lamellar couple). All the position values increase as the eutectic grows. The lamellae change the growth trajectory to adapt to the convection-solute transport. Compared with the symmetric eutectic without convection, the regulated pattern under external perturbations can be considered as a self-adjusting process to accommodate newly established equilibrium.

To further explore how to regulate the eutectic trajectory under external perturbations, complex thermal and convective conditions are applied during eutectic evolution. Figure 3 shows the evolution of the eutectic pattern influenced by two laser spots at (0.25X, 0.5Y) and (0.75X, 0.5Y), where X and Y are the domain width and height, respectively. The boundary conditions and initial settings are similar to those in Fig. 1(a) except that the domain width and height are magnified by three and two times, respectively. Three eutectic colonies with crooked lamellae and curved solid-liquid interfaces can be observed (see movie included in the Supplemental Material (SM) [30]). Figure 3(d) shows the temperature evolution, and Fig. 3(e) shows the solute distribution along the direction designated by the white arrow in Fig. 3(c). The temperature changes in a nonlinear fashion except for the constant maximum temperature (i.e., laser temperature), and the concentration exhibits symmetric fluctuation. The presence of a eutectic colony, which is normally considered to be caused by ternary impurities [31], is predicted here in the pure binary eutectic, which is attributed to the uneven growth dynamics

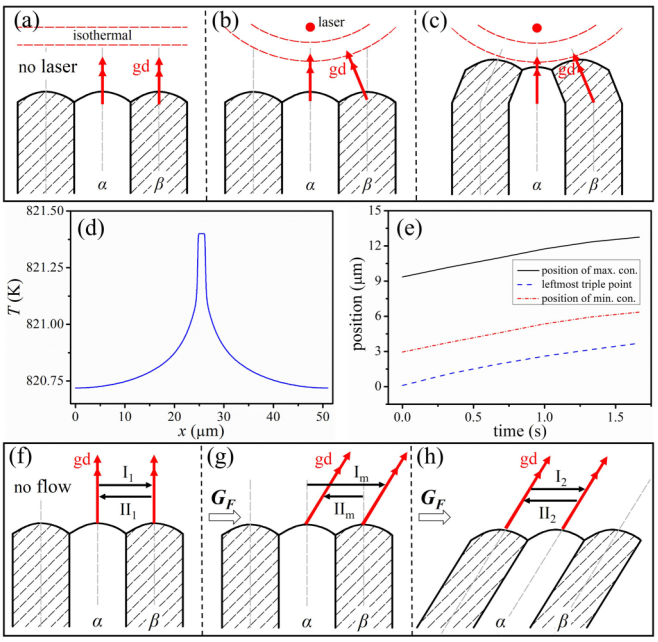

FIG. 2. Illustration of the adjusting mechanism of eutectic lamellae under thermal and convective perturbations. (a)–(c) Schematic diagrams corresponding to the steady state without thermal perturbation, the transient state with thermal perturbation, and the steady state with thermal perturbation, where the term "gd" denotes "growth direction." (d) Temperature vs the distance along the horizontal direction spanning the center of the laser spot in Fig. 1(a). (e) Positions of the concentration extremes and the leftmost triple point vs time after generating the shear flow (focusing on the leftmost lamellar couple). (f)–(h) Schematic diagrams corresponding to the steady state without convection, the transient state with convection, and the steady state with convection.

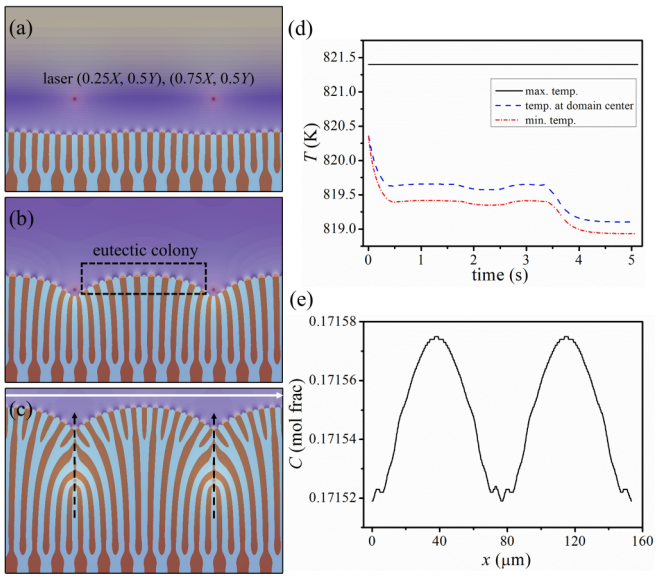

FIG. 3. Evolution of eutectic pattern under two laser spots. (a)–(c) Cloud map of eutectic solute field superimposed on temperature field (see the movie included in the Supplemental Material [30]). The trajectory of the grooves between colonies is marked by the dashed black arrows. (d) Domain temperature vs time. (e) Solute concentration along the direction designated by the white arrow in (c).

induced by the local thermal perturbation. The colony formation is trigged by a morphological instability with lamellae creation and protruding fingers. Deep grooves between neighboring colonies are marked by the dashed black arrows, and their shape continuously changes with the overgrowth event.

To reveal the eutectic regulating under convection, two periodic forces including square and triangular waves are imposed in the undercooled melt. Figure 4 shows the simulated eutectic patterns after six periods where the force period T_f is 16,000,000 steps (5.33 s). The force amplitude is retrieved *via* numerical tests and stays the same for the two force modes. The boundary conditions and initial settings are similar to those in Fig. 1(d) except that the domain height is magnified by eight times. Once the external force changes, the lamellae adjust the growth trajectory rapidly, resulting in a zigzag pattern under square-waving force and a snakelike pattern under triangular-waving force (see movie in the SM [30]). In addition, the effect of convection is more significant under square-waving force, and the average longitudinal growth velocity is 9.6 μm/s, which is less than 10.2 μm/s under triangular-waving force.

The liquid flow induced by the lateral force is similar to Couette flow. The difference is that the flow velocity increases nonlinearly from zero at the solid-liquid interface to the maximum at the domain top. Accordingly, the maximum flow velocity decreases with decreasing remaining liquid height, and the lamellar tilting angle decreases with the eutectic evolution. Figure 4(e) shows the lamellar tilting angle versus time under the two force modes, in which the inset shows the definition of the angle sign. Under the square wave mode, the tilting angle stays constant at each half period, and the absolute magnitude decreases in a step-shape manner. But under the triangular wave mode, the tilting angle decreases continuously as the eutectic evolves.

It is noted that a tilt domain is usually observed during lamellar eutectic growth when a group of asymmetrical cells travel laterally along the growth front and its dynamics is essentially a wavelength-selection problem [7]. The two neighboring walls move along the opposite direction of the tilting direction, and the symmetry-breaking pattern is highly dependent on a combining anisotropy effect, including surface-tension anisotropy, intergrain anisotropy, and capillary anisotropy. In the present work, however, the crystal anisotropy is ignored and the tilt band is caused by the external perturbations. For the convection-solute eutectic growth, all the lamellae tilt towards the same direction, and the wavelength equals the lamellar spacing regardless of the magnitude of flow intensity and undercooling. The consistent behavior among all the lamellae indicates that the mechanism of the tilt band induced by external perturbations is different from that of the spontaneous tilting behavior for the epitaxial locked eutectics and the tilt instability for the floating eutectics [32]. The crystal anisotropy, named the "internal factor," plays a nontrivial role in the dynamical regulating process of both the locked and floating eutectics. But the presence of the external flow field changes the local thermodynamic equilibrium and

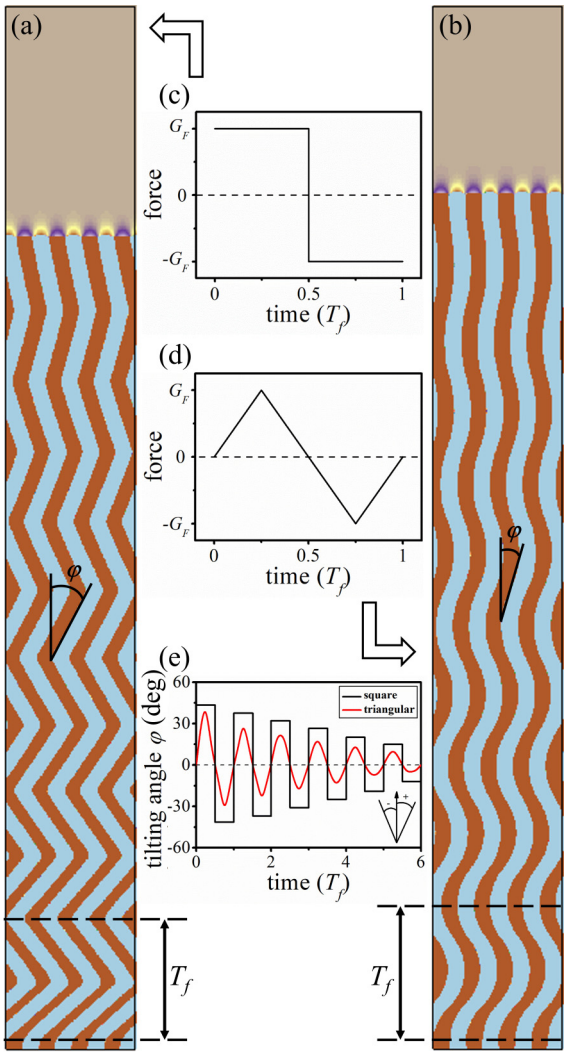

FIG. 4. Simulated eutectic patterns under two periodic external force modes. (a) and (c) are the cloud maps of solute field under square and triangular waves, respectively (see movies in Supplemental Material [30]), and (b) and (d) are the corresponding waveform diagram. (e) Tilting angle vs time under the two force modes including square and triangular waves. The inset shows the definition of the angle sign.

the eutectic morphology by affecting the solute distribution near the growth front, which is independent of the eutectic types and can be considered as an "external factor."

For the thermosolutal eutectic growth, the presence of thermal shock distorts the lamellae by bending the isotherms. Similar to that for the convection-solute eutectic growth, such an external factor changes lamellar growth behavior in a consistent way and the average wavelength is unchanged before lamellae creation occurs. It can be speculated that the combination of the internal and external factors controls the eutectic evolution, and the internal factor becomes predominant under pure or nearly pure conditions without external perturbations.

In summary, the adjustment of the eutectic trajectory under external perturbations is discussed in terms of thermal and convective effects. Compared with the present four viewpoints regarding the cause of the asymmetric eutectic trajectory which is established under the pure diffusion assumption, the eutectic transition due to the presence of the thermal and convective perturbations can be considered as artificially altered external interferences. The presence of thermal perturbation distorts the eutectic lamellae, while the convective perturbation causes a tilt band by changing lateral solute transfer near the growth front. Both can adjust the eutectic trajectory to accommodate a new thermodynamic equilibrium. According to the regulated eutectic colony, zigzag, and snakelike eutectic patterns, it is believed that understanding of the regulating mechanism under external perturbations can help control the eutectic patterns of casting alloys by altering local thermal and/or convective behavior. Besides, using the phase-field lattice-Boltzmann method to investigate eutectic evolution also sheds light on the microstructure prediction under multiphysical fields.

This work is financially supported by the Joint Funds of the National Natural Science Foundation of China (Grant No. U1537202), the Tsinghua-General Motors International Collaboration Project (Grant No. 20153000354), the China Scholarship Council (Grant No. 201906295007), and the Tsinghua Qingfeng Scholarship (Grant No. THQF2018-15). The authors would also like to thank the National Laboratory for Information Science and Technology in Tsinghua University for access to supercomputing facilities.

APPENDIX A: TYPICAL SIMULATION RESULT OF THE THERMO-SOLUTE-CONVECTION EUTECTIC GROWTH

Figure 5 shows the evolution of the eutectic pattern under the coupled thermo-solute-convection condition. The top and bottom rows are the distribution of the solute and temperature, and the black arrows in Figs. 5(a)–5(c) denote the velocity vectors. Both the initial condition and simulation parameters are similar to those in Fig. 1. The eutectic lamellae grow into the undercooled melt with a planar interface. The release of latent heat leads to a local high-temperature region exhibiting at the solid-liquid interface. The melt flows from the α phase

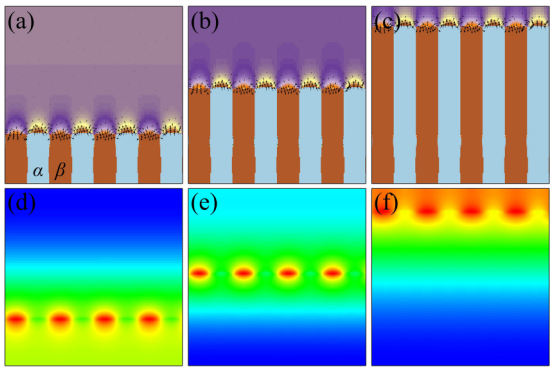

FIG. 5. Evolution of the eutectic pattern under the coupled thermo-solute-convection condition. The top and bottom rows are the distribution of the solute and temperature, and the black arrows in (a)–(c) denote the velocity vectors.

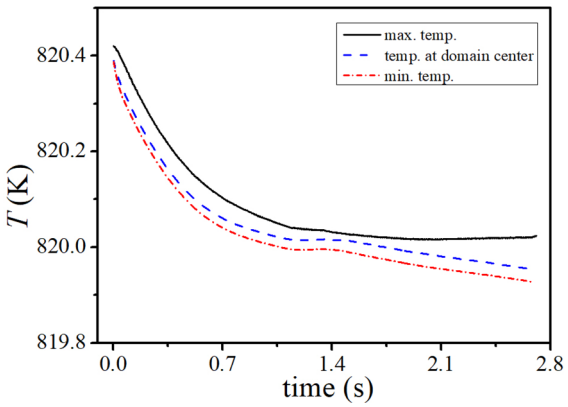

FIG. 6. Domain temperature vs time.

to the β phase, i.e., causing an inflow at the high-density phase (rich-Cu β phase), which agrees with that reported by Coriell *et al.* [33].

Figure 6 shows the domain temperature versus time. The interaction between the latent heat and heat sink decreases the temperature nonlinearly, and a lower temperature corresponds to a faster growth velocity. As an attempt to reveal the multiphysical interaction, the study on the thermo-solute-convection eutectic growth can lay a foundation for further investigation of eutectic growth dynamics.

APPENDIX B: DETAILS OF THE NUMERICAL ALGORITHM

To increase the computational efficiency, a numerical algorithm based on parallel computing and adaptive mesh refinement is developed to solve the multiphysical phase-field equations. A gradient criterion is employed to tag the meshes that require refinement:

$$\max_{1\leqslant i\leqslant 3}(|\nabla\phi_i|) + E_C|\nabla C| + E_T|\nabla T| + E_v(\sqrt{|\nabla u|^2+|\nabla v|^2}) \geqslant \xi, \tag{B1}$$

where E_C, E_T, and E_v are weight coefficients for solute concentration, temperature, and flow velocity, and ξ is a threshold determined through numerical tests.

When local meshes are tagged according to Eq. (B1), refined new and half-sized meshes are generated in those areas. The refinement process is repeated until reaching the finest mesh level. During the mesh reconstruction, a cluster algorithm is used to pack the newly generated meshes into patchboxes. The layout of the patchboxes, together with meshes and computing data, is then dispatched to all processes to achieve the so-called load balance for parallel computing (using MPI). Successful implementation can be referred to in [34] for thermosolutal eutectic growth and in [24] for convection-solute eutectic growth.

[1] J. A. Dantzig and M. Rappaz, *Solidification* (EPFL Press, Lausanne, 2009).
[2] A. Zhang, J. Du, Z. Guo, Q. Wang, and S. Xiong, Scripta Mater. **165**, 64 (2019).
[3] S. Akamatsu, K. Lee, and W. Losert, J. Cryst. Growth **289**, 331 (2006).
[4] H. E. Cline, Mater. Sci. Eng. **65**, 93 (1984).
[5] A. Karma and A. Sarkissian, Metall. Mater. Trans. A **27**, 635 (1996).
[6] G. Faivre and J. Mergy, Phys. Rev. A **45**, 7320 (1992).
[7] G. Faivre and J. Mergy, Phys. Rev. A **46**, 963 (1992).
[8] S. Akamatsu, S. Bottin-Rousseau, M. Şerefoğlu, and G. Faivre, Acta Mater **60**, 3199 (2012).
[9] S. Akamatsu, S. Bottin-Rousseau, M. Şerefoğlu, and G. Faivre, Acta Mater **60**, 3206 (2012).
[10] U. Hecht, L. Gránásy, T. Pusztai, B. Böttger, M. Apel, V. Witusiewicz, L. Ratke, J. De Wilde, L. Froyen, D. Camel, B. Drevet, G. Faivre, S. G. Fries, B. Legendre, and S. Rex, Mater. Sci. Eng., R **46**, 1 (2004).
[11] M. Apel, B. Böttger, V. Witusiewicz, U. Hecht, and I. Steinbach, Lamellar pattern formation during 2d-directional solidification of ternary eutectic alloys, in *Solidification and Crystallization*, edited by D. M. Herlach (Wiley-VCH Verlag GmbH & Co. KGaA, Weinheim, 2004).
[12] J. Hötzer, P. Steinmetz, M. Jainta, S. Schulz, M. Kellner, B. Nestler, A. Genau, A. Dennstedt, M. Bauer, H. Köstler, and U. Rüde, Acta Mater **106**, 249 (2016).
[13] X. Li, Z. Ren, Y. Fautrelle, Y. Zhang, and C. Esling, Acta Mater **58**, 1403 (2010).
[14] J. C. Ramirez, C. Beckermann, A. Karma, and H. J. Diepers, Phys. Rev. E **69**, 051607 (2004).
[15] T. Haxhimali, A. Karma, F. Gonzales, and M. Rappaz, Nat. Mater. **5**, 660 (2006).
[16] R. Folch and M. Plapp, Phys. Rev. E **72**, 011602 (2005).
[17] M. Şerefoğlu, R. E. Napolitano, and M. Plapp, Phys. Rev. E **84**, 011614 (2011).
[18] T. Krüger, H. Kusumaatmaja, A. Kuzmin, O. Shardt, G. Silva, and E. M. Viggen, *The Lattice Boltzmann Method, Principles and Practice* (Springer, Cham, Switzerland, 2017).
[19] A. Zhang, J. Du, Z. Guo, Q. Wang, and S. Xiong, Metall. Mater. Trans. B **50**, 517 (2019).
[20] A. Zhang, J. Du, Z. Guo, and S. Xiong, Phys. Rev. E **98**, 043301 (2018).
[21] T. Seta, Phys. Rev. E **87**, 063304 (2013).
[22] A. Zhang, J. Du, Z. Guo, Q. Wang, and S. Xiong, Metall. Mater. Trans. B **49**, 3603 (2018).
[23] C. Beckermann, H. J. Diepers, I. Steinbach, A. Karma, and X. Tong, J. Comput. Phys. **154**, 468 (1999).
[24] A. Zhang, Z. Guo, and S. M. Xiong, Phys. Rev. E **97**, 053302 (2018).
[25] R. Siquieri and H. Emmerich, Philos. Mag. **91**, 45 (2011).
[26] W. M. Wang, Z. G. Liu, J. M. Liu, and X. Y. Chen, J. Cryst. Growth **240**, 313 (2002).
[27] J. H. Lee, S. Liu, and R. Trivedi, Metall. Mater. Trans. A **36**, 3111 (2005).
[28] J. M. Quenisset and R. Naslain, J. Cryst. Growth **54**, 465 (1981).
[29] V. Baskaran and W. R. Wilcox, J. Cryst. Growth **67**, 343 (1984).

[30] See Supplemental Material at http://link.aps.org/supplemental/10.1103/PhysRevE.101.061301 for the movies including the evolution of eutectic pattern under two laser spots, the evolution of eutectic pattern under square wave force mode, and the evolution of eutectic pattern under triangular wave force mode.

[31] M. Plapp and A. Karma, Phys. Rev. E **66**, 061608 (2002).

[32] B. Caroli, C. Caroli, G. Faivre, and J. Mergy, J. Cryst. Growth **118**, 135 (1992).

[33] S. R. Coriell, G. B. McFadden, W. F. Mitchell, B. T. Murray, J. B. Andrews, and Y. Arikawa, J. Cryst. Growth **224**, 145 (2001).

[34] A. Zhang, F. Liu, J. Du, Z. Guo, Q. Wang, and S. Xiong, Int. J. Heat Mass Transfer **145**, 118778 (2019).